# Balanced and Unbalanced Routes to Dissipation in an Equilibrated Eady Flow

**M. Jeroen Molemaker, James C. McWilliams, and Xavier Capet**
**IGPP, UCLA**

(Received 6 February 2008)

The oceanic general circulation is forced at large scales and is unstable to mesoscale eddies. Large-scale currents and eddy flows are approximately in geostrophic balance. Geostrophic dynamics is characterized by an inverse energy cascade except for dissipation near the boundaries. In this paper we confront the dilemma of how the general circulation may achieve dynamical equilibrium in the presence of continuous large-scale forcing and the absence of boundary dissipation. We do this with a forced horizontal jet with spatially uniform rotation, vertical stratification, and vertical shear in a horizontally periodic domain, *i.e.,* a version of Eady's (1949) flow carried to turbulent equilibrium. A direct route to dissipation is presented that is essentially non-geostrophic in its dynamics, with significant submesoscale frontogenesis, frontal instability and breakdown, and forward kinetic energy cascade to dissipation. To support this conclusion a series of simulations is made with both Quasigeostrophic and Boussinesq models. The Quasigeostrophic model is shown as incapable of equilibration at increasingly higher numerical resolution (hence Reynolds number), whereas the non-geostrophic Boussinesq model equilibrates with only weak dependences on resolution and Rossby number.

## 1. Introduction

The general circulations of the atmosphere and ocean are forced at large scales, and to achieve equilibrium they must viscously dissipate much of their kinetic energy at small scales. The prevailing dynamical paradigm for large and mesoscale flows includes diagnostic force-balance constraints, *i.e.,* hydrostatic and either geostrophic or some form of gradient-wind balances (McWilliams 2003). A related paradigm is the inverse energy cascade of geostrophic turbulence (Charney 1971). Together these imply a potential dilemma for energy equilibration (Muller *et al.* 2005): if the directly forced large-scale flow loses energy by instability to balanced mesoscale eddies, then how is the eddy energy viscously dissipated if it is transferred only toward larger scales? Part of the dissipation can occur in the top or bottom turbulent boundary layers, but unless energy flux from the interior to the boundary is efficient enough, this route may not suffice. In this paper we examine the possibility of a direct route to dissipation in the interior by a forward energy cascade involving a spontaneous violation of the diagnostic force-balance constraints.

We pose the highly idealized problem of an equilibrium Eady flow with a restoring forcing toward a uniformly stratified, uniform vertical shear flow in a uniformly rotating environment. This "large-scale" flow has linear baroclinic instability modes, both force-balanced (Eady 1949) and anticyclonic ageostrophic (Stone 1966; Molemaker *et al.* 2005). The boundary conditions are horizontal periodicity and solid vertical boundaries with no stress or buoyancy flux (*i.e.,* with no representation of turbulent boundary layers). Fluc-

tuations amplify through these instabilities and equilibrate only by viscous dissipation. The fluid dynamical model is the incompressible Boussinesq equations (BOUS).

This posing is designed to produce a crisis in the sense that the fluctuation energy will continue to grow as the Reynolds number $Re$ increases unless a forward energy cascade arises to provide an efficient "interior" route to dissipation. The problem is solved in a parameter space with both $Re$ and the Rossby number $Ro$ as control parameters. To provide a comparison dynamical standard, we also solve the equivalent problem with the force-balanced Quasigeostrophic equations (QG), which is the asymptotic model as $Ro \to 0$ (Pedlosky 1987) where no forward cascade is expected.

This problem has a different focus compared to recent studies of randomly forced stratified turbulence by, among others, Lindborg (2005); Waite and Bartello (2006). In those problems there is a a vigorous forward energy cascade, and $Ro$ is decreased from large values until a certain degree of inverse energy cascade begins at an $O(1)$ threshold value. Our approach is very different and focuses on the strength of the forward cascade at $Ro \to 0$. In other words, instead of focusing on the emergence of an inverse energy cascade as $Ro$ is reduced, we study the emergence of a forward energy cascade as the $Ro$ is increased from zero to small, finite values.

Section 2 explains the model formulation and solution methods. Section 3 presents solutions for the unforced spin-down of an Eady flow, and Sec. 4 presents equilibrium solutions. Section 5 analyzes departures from diagnostic force balances and their relation to forward energy cascade and fine-scale instability of density fronts. Conclusions are in Sec. 6.

## 2. Formulation and Methods

We pose the problem as the nonlinear evolution of fluctuations around a mean horizontal current $V(z)\hat{\mathbf{y}}$ in geostrophic, hydrostatic balance for a rotating, stably stratified fluid with Coriolis frequency $f(y) > 0$ and Brunt-Vaisalla or buoyancy frequency $N(z) > 0$. To focus on our primary issue, we assume here that $f$, $N$, and $d_z V$ are spatially uniform, even though their variations are important for realistic, large-scale currents. Similarly we ignore horizontal variations in $V$. Boundary layers are avoided by assuming horizontal periodicity with zero horizontal average for the fluctuation fields and solid vertical boundaries without any momentum or heat flux. The price we must pay for simplicity of this degree of spatial homogeneity is that the mean flow and stratification are artificially maintained in the face of their depletion by eddy fluxes. Since our focus is on possible departures from balanced dynamics, we will use BOUS fpr the fundamental fluid dynamics of an incompressible fluid. The problem considered is therefore a non-geostrophic, non-hydrostatic generalization of the linear stability analysis in Eady (1949) and an extension of the further stability analysis in Stone (1966, 1970). Since an important goal is to assess the degree and importance of loss of diagnostic force balance with respect to both the geostrophic and hydrostatic approximations, this investigation continues the instability analysis in Molemaker *et al.* (2005) into the turbulent equilibrium regime.

We derive non-dimensional equations using the following scales for the mean state and fluctuation quantities: horizontal domain width $L$; vertical domain height $H$; horizontal velocity $V_0$; time $L/V_0$; Coriolis frequency $f$; dynamic pressure $\rho_o f V_0 L$; mean and total buoyancy $N^2 H$; fluctuation buoyancy $f V_0 L/H$; vertical velocity $f V_0^2/N^2 H$; and energy density $V_0^2$. As a result several non-dimensional parameters appear: Rossby number $Ro = V_0/fL$; Froude number $Fr = V_0/NH$; aspect ratio $\lambda = H/L$; and $\epsilon = fLV_0/N^2H^2 = Fr^2/Ro$. This non-dimensionalization follows McWilliams (1985), and it is designed to

expose the generally weak deviations of the flow from balance when these four parameters are not large.

The non-dimensional profiles for the mean meridional velocity and buoyancy field are

$$\begin{aligned} V(z) &= S(t)\,\left(z-\frac{1}{2}\right) \\ B(x,z) &= \int_0^z \gamma(z,t)\,dz + \epsilon S(t)\,\left(x-\frac{1}{2}\right)\,, \end{aligned} \tag{2.1}$$

where $S$ is the mean vertical shear, $\gamma$ is the mean stratification (*i.e.,* square of the buoyancy frequency), and the domain is $[0,1]$ in each coordinate. The associated mean zonal and vertical velocities are zero. $S=\gamma=1$ is Eady's flow. In conservative dynamics the potential vorticity is a Lagrangian invariant, and its distribution is relevant to possible flow instabilities. For BOUS (Sec. 2.1), the Ertel potential vorticity (non-dimensionalized by $fN^2$) for the mean state is

$$\prod\nolimits_m \;= \gamma - Ro\epsilon S^2 \;\le\; \gamma\,. \tag{2.2}$$

The inequality indicates that $\prod_m$ has an anticyclonic constant value for Eady's flow. For QG (Sec. 2.2), the relevant mean potential vorticity $q_m$ is zero.

### 2.1. *Boussinesq Model*

The governing non-dimensional equations for the fluctuations about the mean state (2.1) in BOUS are

$$\begin{aligned} Ro\,(\partial_t u + N[u] + V\partial_y u) - v &= -\partial_x p + \frac{Ro}{Re}\nabla^2 u \\ Ro\,(\partial_t v + N[v] + V\partial_y v + \epsilon w\partial_z V) + u &= -\partial_y p + \frac{Ro}{Re}\nabla^2 v \\ Fr^2\lambda^2\,(\partial_t w + N[w] + V\partial_y w) &= -\partial_z p + b + \frac{\epsilon Ro\lambda^2}{Re}\nabla^2 w \\ \partial_x u + \partial_y v + \epsilon\partial_z w &= 0 \\ \partial_t b + N[b] + V\partial_y b + uS + w\gamma &= \frac{Pr}{Re}\nabla^2 b\,, \end{aligned} \tag{2.3}$$

together with the boundary conditions of $w=0$ at $z=0,1$ and horizontal periodicity with a zero average for all fluctuation quantities. Here $u$, $v$, and $w$ are cross-stream, downstream, and vertical fluctuation velocity components; $b$ is fluctuation buoyancy; and $p$ is fluctuation pressure. We use a compact notation for self-advection of a fluctuation quantity $a$,

$$N[a] \;=\; \partial_x[ua] + \partial_y[va] + \epsilon\partial_z[wa - \overline{wa}]\,,$$

where the overbar is a horizontal average. The definition of Reynolds and Prandtl numbers are the usual ones,

$$Re \;=\; \frac{\nu}{V_0 L} \quad \text{and} \quad Pr \;=\; \frac{\nu}{\kappa}\,,$$

and we choose $Pr=1$ for all cases. Explicit diffusion (hence dissipation) is incorporated into the model by means of the Laplacian operator $\nabla^2$. In addition to this, the upwind weighted discretization of the advection operator provides additional numerical dissipation.

The total discrete, numerical and explicit, dissipation is diagnosed using a discrete equation for kinetic energy, analogous to (2.8). That way, the integral (and spectral, see

4.3) effect of each term in the momentum equation can be computed. For instance, the domain integrated dissipative effect of advection can be computed as:

$$D_{adv} = \int\int\int \mathbf{u} \cdot (\mathbf{u} \cdot \nabla \mathbf{u}) \; dx \; dy \; dz \, . \tag{2.4}$$

For a non-dissipative advection scheme, $D_{adv}$ will be identically zero. Using an upwind weighted advection scheme, $D_{adv} < 0$. By comparing $D_{adv}$ with $D_{visc} = \mathbf{u} \cdot \nabla^2 \mathbf{u}$, we can assess the relative importance of each for the total dissipation. For all results, the explicit viscosity is chosen such that numerical and explicit dissipation are roughly equal. This estimation is used to compute an approximate Reynold number for the flows computed. The viscosity used to compute the approximate $Re$ is the explicit value, multiplied by the ratio of total dissipation and explicit dissipation (also see Secs. 2.3 and 4.3).

To accompany the fluctuation evolution (2.3), we require equations for the mean quantities $S(t)$ and $\gamma(z,t)$. Since (2.1) is not strictly consistent with either horizontal periodicity nor an infinite horizontal extent, this requires a closure hypothesis comprised of two parts: buoyancy and energy balances in the fluctuation–mean interactions, and forcing terms that act to restore the evolving flow toward Eady's flow.

Buoyancy balance is expressed as a horizontal average of the vertical derivative of the non-dimensional total buoyancy equation at each level, excluding vertical diffusion and including a restoring tendency:

$$\frac{\partial \gamma}{\partial t} \;=\; -\,\epsilon^2 \partial_{zz} \overline{wb} \; + \alpha_\gamma (1-\gamma) \, , \tag{2.5}$$

where $\alpha_\gamma$ is a restoring coefficient. Buoyancy terms involving $S$ do not contribute because they are antisymmetric in $x$ in (2.1) and vanish in a horizontal average. This determines the evolution of $\gamma(z,t)$ after evaluating $\overline{wb}$ from the fluctuation fields.

The kinetic energy density for the mean flow is $E_{km} = \frac{1}{2} V^2$, and its volume integral for $V(z)$ in (2.1) is

$$\mathcal{E}_{km} \;\equiv\; \overline{\langle E_{km} \rangle} \;=\; \frac{S^2}{24} \, , \tag{2.6}$$

where the angle brackets denote a vertical integral (also equal to a vertical average in a domain of unit height). The fluctuation equations (2.3) have an integral kinetic energy conservation law for

$$E_{kf} = \frac{1}{2} \left( u^2 + v^2 + \epsilon^2 \lambda^2 w^2 \right) \; ; \tag{2.7}$$

*viz.,*

$$\frac{d\mathcal{E}_{kf}}{dt} = \frac{\epsilon}{Ro} \overline{\langle wb \rangle} - \epsilon \, \overline{\langle vw \rangle} \, S - D_f \, , \tag{2.8}$$

with $\mathcal{E}_{fk} = \overline{\langle E_{fk} \rangle}$ and an explicit dissipation rate,

$$D_f \;=\; \frac{1}{Re} \overline{\langle (\boldsymbol{\nabla} u)^2 + (\boldsymbol{\nabla} v)^2 + \epsilon^2 \lambda^2 (\boldsymbol{\nabla} w)^2 \rangle} \, .$$

Lorenz (1955) demonstrated that the energy exchange between a zonal mean flow $S$ and its fluctuations is most cogently described in terms of conservation of kinetic $\mathcal{E}_k$ plus available potential $\mathcal{E}_a$ energies (rather than total potential energy, which in our problem is a function only of $\gamma$, not the mean flow $S$). Accordingly, we adopt the energy closure principle to determine the evolution of $S(t)$; *i.e.,*

$$\frac{d(\mathcal{E}_{km} + \mathcal{E}_{kf} + \mathcal{E}_a)}{dt_{adv}} = 0 \tag{2.9}$$

for the mean-fluctuation interaction terms, neglecting all diffusive terms of $\mathcal{O}(Re^{-1})$ for the mean flow and stratification. $\mathcal{E}_a$ is formally defined as the difference in the potential energy $\mathcal{E}_p$ of a given 3D buoyancy field and the reference (lowest) potential energy $\mathcal{E}_{\surd ref}$ that could be reached by an adiabatic rearrangement of parcels into a horizontally uniform field with non-negative vertical buoyancy gradient:

$$\mathcal{E}_a = \mathcal{E}_p - \mathcal{E}_{p_{ref}} \,. \tag{2.10}$$

In BOUS no analytical expression for $\mathcal{E}_a$ is known; nevertheless, following Winters *et al.* (1995), we introduce an operational procedure for determining $\mathcal{E}_a$ and its derivatives from the buoyancy field Molemaker and McWilliams (2008). Furthermore, we can decompose $\mathcal{E}_a$ into mean an fluctuation contributions by

$$\mathcal{E}_a = \mathcal{E}_{am} + \mathcal{E}_{af} \,, \tag{2.11}$$

where $\mathcal{E}_{am}$ is evaluated using only the mean buoyancy field ($\gamma$, $S$) and $\mathcal{E}_{af}$ is evaluated by residual. Since $\mathcal{E}_a$ is a functional of $\gamma$, $S$, and $b$, we evaluate its time derivative by

$$\frac{d\mathcal{E}_a}{dt} \;=\; \frac{\delta\mathcal{E}_a}{\delta\gamma}\cdot\frac{\partial\gamma}{\partial t} + \frac{\delta\mathcal{E}_a}{\delta S}\cdot\frac{dS}{dt} + \frac{\delta\mathcal{E}_a}{\delta b}\cdot\frac{\partial b}{\partial t} \,. \tag{2.12}$$

The $\delta$ symbol denotes a functional derivative. The dots are vector products with the functional argument (*n.b.,* $S$ is zero dimensional, $\gamma(z)$ is 1D, and $b(x,y,z)$ is 3D). Thus the vector products in (2.12) are equivalent to volume integrals in the unit cube. In practice the functional derivatives are calculated by finite differences (as in the rest of the numerical model; Sec. 2.3); *e.g.,*

$$\frac{\delta\mathcal{E}_a}{\delta S} \;=\; \frac{\mathcal{E}_a[\gamma,\, S+0.5\mu,\, b] - \mathcal{E}_a[\gamma,\, S-0.5\mu,\, b]}{\mu} \,, \tag{2.13}$$

with $\mu$ a small number but large enough to avoid floating-point precision errors. By combining (2.3), (2.6), (2.8), (2.9), and (2.12) with respect to their conservative dynamical terms, we obtain

$$\begin{aligned}\left(\frac{S}{12}+\frac{\delta\mathcal{E}_a}{\delta S}\right)\left(\frac{dS}{dt}-\alpha_S\,(1-S)\right) \;=\; & -\frac{\epsilon}{Ro}\overline{\langle wb\rangle} + \epsilon\,\overline{\langle vw\rangle}\,S \\ & + \frac{\delta\mathcal{E}_a}{\delta\gamma}\cdot\left(\epsilon^2\partial_{zz}\overline{wb}\right) + \frac{\delta\mathcal{E}_a}{\delta b}\cdot\left(N[b] + V\partial_y b + Su + w\gamma\right) \,.\end{aligned} \tag{2.14}$$

The set of (2.3, (2.5), and (2.14) provides a well-posed system for the evolution of the mean state and fluctuations. In Sec. 2.2 we show that this system is asymptotically consistent with the more familiar QG model where $\mathcal{E}_a$ and its derivatives are analytically specifiable (Molemaker and McWilliams 2008).

With this representation the total, non-dimensional Ertel potential vorticity is defined by the following vector product between the absolute vorticity and the buoyancy gradient:

$$\begin{aligned}\prod = & \left(\frac{Ro}{\lambda}\left[-S-\partial_z v + Fr^2\lambda^2\partial_y w\right] \,,\; \frac{Ro}{\lambda}\left[\partial_z u - Fr^2\lambda^2\partial_x w\right] \,,\; 1 + Ro\left[\partial_x v - \partial_y u\right]\right) \\ & \cdot \;\left(\,\epsilon\lambda(S+\partial_x b)\,,\; \epsilon\lambda\partial_y b\,,\; \gamma+\epsilon\partial_z b\,\right) \,.\end{aligned} \tag{2.15}$$

The fluctuation potential vorticity is $\prod_f = \prod - \prod_m$. In the absence of forcing and dissipative effects, $\prod$ is conserved following the flow. Since the initial and mean states have no interior $\prod$ gradients, the fluctuations do not inherit any $\prod$ variations through the instability generation process. However, the model equations do not exactly conserve $\prod$ in their discrete form, and diffusive effects can introduce $\prod$ fluctuations in the flow,

mainly on small scales. Due to the tendency of $\prod$ to homogenize on horizontal or isopycnal surfaces by eddy mixing (Rhines and Young 1982), we expect its interior gradients to remain small and find that this is generally so.

### 2.2. *Quasigeostrohic Model*

Starting with (2.3), take the curl of the horizontal momentum equations; use the hydrostatic approximation; add the vertical derivative of the buoyancy equation; discard all terms that are asymptotically small in $Ro$, $Fr$, and $\epsilon$; and neglect vertical diffusion. The result is the non-dimensional, QG potential vorticity equation for the fluctuations, including horizontal diffusion:

$$[\partial_t + V\partial_y]q + J_h(\Psi, q) = \frac{1}{Re}\nabla_h^2 q\,,$$
$$\text{where} \quad q \;=\; \nabla_h^2\Psi + \frac{\epsilon}{Ro}\,\partial_{zz}\Psi\,. \tag{2.16}$$

Here $q$ is the fluctuation potential vorticity, and $\Psi$ is the geostrophic streamfunction with $u = -\partial_y\Psi,\ v = \partial_x\Psi$. The subscript $h$ denotes a horizontal Laplacian operator. The vertical velocity is $w = -[\partial_t + V\partial_y]\partial_z\Psi + J_h(\Psi, \partial_z\Psi)$, and the buoyancy is $b = \partial_z\Psi$. Boundary conditions at $z = 0, 1$ are

$$[\partial_{tz} + V\partial_{zy}]\Psi + J_h(\Psi, \partial_z\Psi) - S\partial_y\Psi \;=\; \frac{1}{Re}\nabla_h^2\partial_z\Psi\,. \tag{2.17}$$

Due to the linear homogeneous operator form of the potential vorticity equation in (2.16), $q$ will remain zero at all times if it is initially zero. This is the class of solutions we focus on. For QG solutions with $q = 0$ in the interior, the dynamics is that of two coupled surface quasigeostrophic models (SQG), each one representing the buoyancy advection-diffusion dynamics at one of the vertical boundaries (Held *et al.* 1995). Baroclinic instability is permitted through the coupling of vertical edge waves Eady (1949). For horizontal scales small compared to $L_r$ (the first-baroclinic deformation radius), the coupling is weak, and the dynamics reduces to uncoupled SQG models associated with each of the boundaries boundaries. Thus, the structure of the turbulent flow at submesoscales is not inconsistent with Held *et al.* (1995).

In QG $\gamma$ remains fixed at its Eady value of one since its eddy-induced evolution rate is $\mathcal{O}(\epsilon^2)$ in (2.5). An energy equation for the fluctuations is obtained by multiplying (2.16) by $-\Psi$ and integrating over the domain. After using the boundary conditions and making several integrations by parts, we obtain the following:

$$\frac{d\mathcal{E}_{qf}}{dt} = -\,\frac{\epsilon}{Ro}\,S\,\overline{\langle\partial_y\Psi\partial_z\Psi\rangle} - \frac{1}{Re}\left[\overline{(\nabla_h^2\Psi)^2 + \frac{\epsilon}{Ro}(\partial_z\nabla_h\Psi)^2}\right],$$
$$\mathcal{E}_{qf} \;=\; \frac{1}{2}\overline{\langle(\partial_x\Psi)^2 + (\partial_y\Psi)^2 + \frac{\epsilon}{Ro}(\partial_z\Psi)^2\rangle}\,. \tag{2.18}$$

The first term in $\mathcal{E}_{qf}$ is the QG approximation to $\mathcal{E}_{kf}$, and the second term is the contribution of the buoyancy fluctuations to $\mathcal{E}_a$. The corresponding expression for the mean QG energy is

$$\mathcal{E}_{qm} \;=\; \frac{S^2}{24}\left(1 + \frac{\epsilon}{Ro}\right), \tag{2.19}$$

again a sum of $\mathcal{E}_{km}$ and the mean-flow contribution to $\mathcal{E}_{am}$. (This expression is consistent with (2.18) for a mean streamfunction $\Psi_m = S(z - \frac{1}{2})\,(x - \frac{1}{2})$.) With a closure principle of conservation of $\mathcal{E}_{qf} + \mathcal{E}_{qm}$ with respect to fluctuation–mean conversion terms, plus a

restoring force toward Eady's flow, the QG equation for $S(t)$ is

$$\frac{S}{12}\left(1+\frac{\epsilon}{Ro}\right)\left(\frac{dS}{dt}-\alpha_S\left(1-S\right)\right) \;=\; \frac{\epsilon}{Ro}\,S\,\overline{\langle\partial_y\Psi\partial_z\Psi\rangle}\,. \tag{2.20}$$

This formulation assures that QG is the limiting form of BOUS as $Ro \to 0$.

### 2.3. *Computational Methods*

The code for BOUS uses finite-difference discretization. It has previously been used to compute laboratory scale flows (Molemaker *et al.* 2000) and atmospheric and ocean flows at scales of tens of kilometers (Molemaker and Vilá-Guerau de Arellano 1998; Molemaker and Dijkstra 2000). It uses a QUICK algorithm for advection of velocities and scalars (Leonard 1979). The QUICK scheme approximates fluxes across cell boundaries with 3rd order accuracy and introduces a small amount of numerical dissipation.

The model has no normal flow at $z = 0$ and 1 and periodic boundary conditions in the horizontal directions. A multigrid Poisson solver allows it to run efficiently on large grids. A third-order Adams-Bashfort scheme is used to advance the variables in time. The QUICK scheme is commonly used in situation where minimal overall dissipation is desired (*e.g.,* Shchepetkin and McWilliams (1998)) and provides dissipation that is more scale selective than a Laplacian viscosity. In (2.10) the evaluation of the reference potential energy $\mathcal{E}_{p_{ref}}$, the lowest potential energy that can be reached through adiabatic rearrangement, is done with an efficient heap sort Press *et al.* (1986) of the discretized buoyancy field.

The QG code is designed as a companion to the BOUS code. It advances (2.16) in the interior and (2.17) for $\partial\Psi/\partial z$ at the top and bottom boundaries. Like its BOUS, it employs central differences for the Laplacian operator, a QUICK algorithm for the advective terms, and an Adams-Bashfort scheme for time stepping.

In both codes the total diffusive effects are a combination of the explicit diffusion operators in (2.3) and (2.16) plus the implicit non-conservative effect of the QUICK algorithm that leads to a dissipation that is somewhat more scale selective than the Laplacian diffusion operator. To diagnose the contribution from the latter, we can compare the QUICK advection term with a centered, second-order scheme that is non-dissipative. Spectral energy balances (Sec. 4.3) are used to verify the correctness of these estimates. The total amount of dissipation is kept to a minimum since we want to study the capacity of the solutions to reach the smallest dissipative scales. The minimal dissipation necessary to maintain numerical stability is a function of grid resolution. The explicit diffusion coefficient is reduced with increasing resolution to allow increasing $Re$ values while still maintaining smoothness on the grid scale, and this reduction occurs automatically with QUICK. The highest resolution used is a $512 \times 512 \times 64$ grid, corresponding to an estimated Reynolds number of $Re = 6600$.

## 3. Spin-Down

To illustrate the behavior of our formulation for mean-state evolution, we examine a set of spin-down experiments with no restoring forcing and initially small fluctuations. Companion solutions are computed using BOUS and QG, and the standard BOUS case has the rather large values of $Ro = 0.5$ and $Fr = 1.6$. When $Ro$ is varied (Sec. 4), its $Ro/Fr$ ratio is held constant. For all solutions $\lambda = 0.1$, and the non-dimensional, first-baroclinic Rossby deformation radius for the initial state is $L_r = 0.1$.

During the initial phase of the evolution, the mean state is baroclinically unstable and loses energy to the fluctuations primarily at horizontal wavenumber $k = 2$ (*i.e.,* a radian

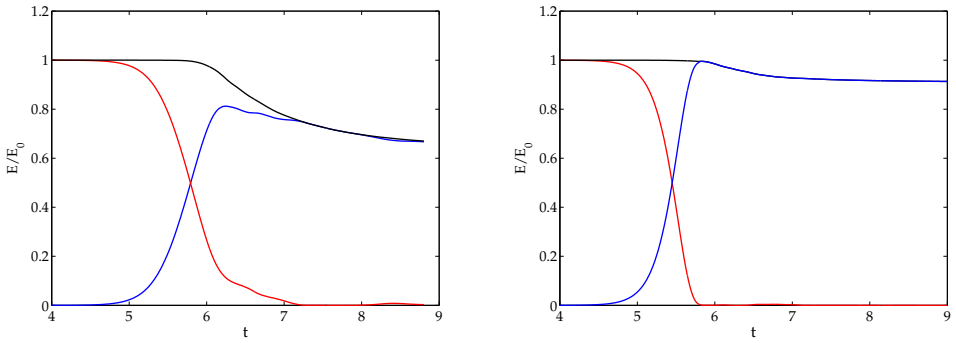


FIGURE 1. Evolution of total energy (kinetic plus available potential) in spin-down ($Re = 2200$): (top) BOUS ($Ro = 0.5$); (bottom) QG. Blue is the fluctuation energy; red is the basic-state energy; and black is the total energy. Towards the end of the simulation, all the kinetic and available potential energy from the basic state is depleted, and the fluctuations have evolved toward a flow structure that fills the domain and is only weakly dissipative.

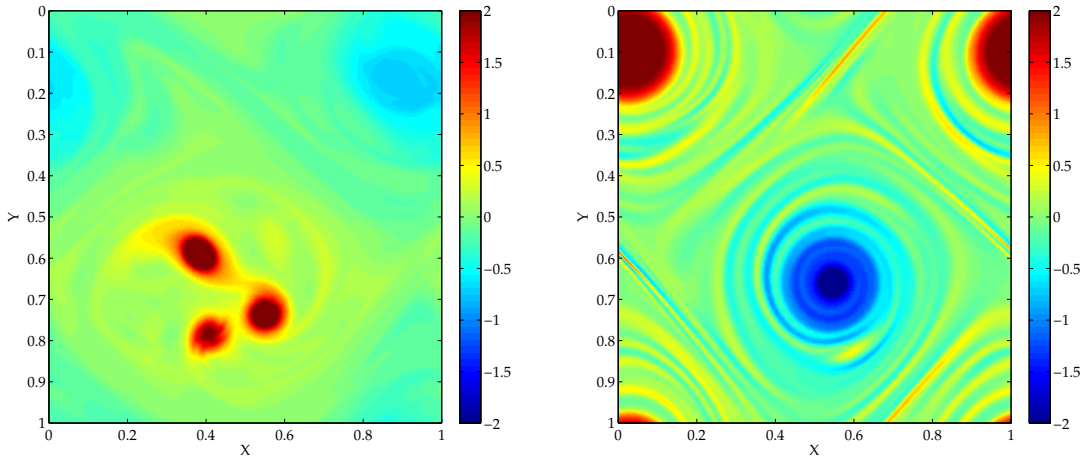


FIGURE 2. Vertical vorticity $\zeta^z(x, y)$ at $t = 9$ and $z = 0.5$ in spin-down ($Re = 2200$): (left) BOUS ($Ro = 0.5$), where the fluctuations have evolved to a set of co-rotating cyclonic eddies; (right) QG, where the fluctuations have evolved to a dipole vortex structure.

length scale of $L = 1/4\pi = 0.08$; Fig. 1). Due to the small wavenumber of the unstable perturbation, the solution is initially only weakly dissipative, and the sum of mean and fluctuation energy is conserved through (2.9) with (2.14) and (2.20). After a period of transition, the mean state is depleted ($S \to 0$), and the fluctuations continue to evolve without further energy input.

After the fluctuations reach large amplitude and self-advection matters, there is a period of intense frontogenesis in both BOUS and QG. Frontogenesis by a deformation field acting to sharpen the buoyancy gradients leads to a restratifying secondary circulation around the front that converts potential to kinetic energy (Hoskins and Bretherton 1972). This process is reflected in energization of small-scale flow components and increased dissipation rate. At the same time an inverse cascade of fluctuation energy occurs and leads to the formation of domain-filling vortices. A quasi-steady end-state for the freely decaying fluctuations is dominated by the large-scale vortices that have little further energy

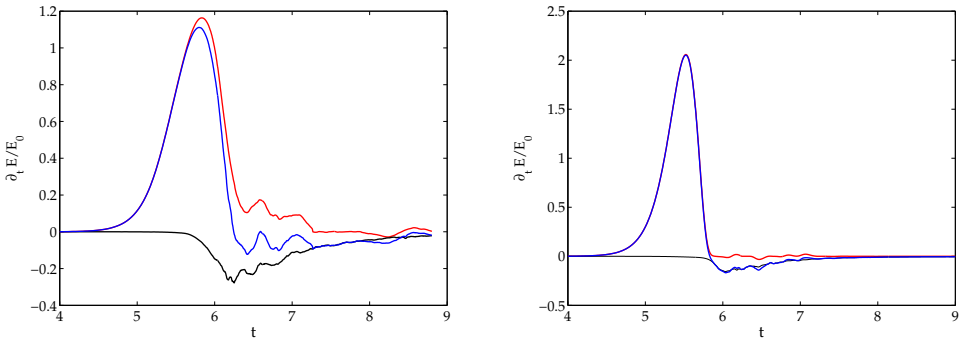


FIGURE 3. Energy balance for the fluctuations in spin-down ($Re = 2200$): (left) BOUS ($Ro = 0.5$); (right) QG. Blue is the the total rate of change of the fluctuations; red is the energy flux from mean to fluctuations; and black is the dissipation of fluctuation energy.

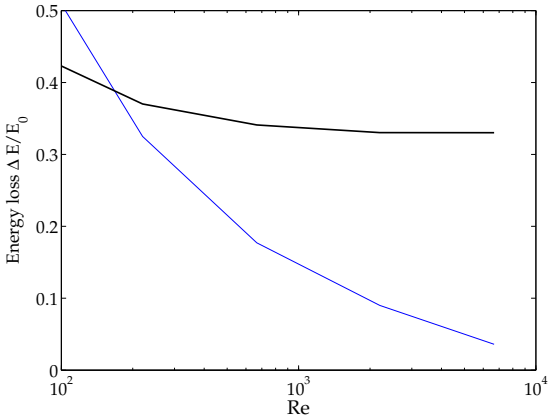


FIGURE 4. Total energy loss during spin-down for different values of $Re$: BOUS ($Ro = 0.5$, black) and QG (blue).

cascade and weak dissipation. Snapshots of vorticity at $z = 0.5$ are in Fig. 2 for times corresponding to these end states. The occurrence and disappearance of small scales, evidenced by a period of enhanced dissipation, is the result of a complicated process of frontogenesis, frontal instability, inverse and forward energy cascades, and selective dissipation of small scales (further discussed in Secs. 4-5). The outcome of these processes is clearly seen in the difference in energy between the initial and end states (Fig. 1).

Figure 3 shows the energy transfer from the mean flow to fluctuations and dissipation during spin-down with an energy budget for the fluctuations. The rate of change of fluctuation energy indicates initial growth of the fluctuations when the mean state is unstable and baroclinic instability sets in. This is also evident from the energy transfer from mean to fluctuations that indicates a continuing energy source for the fluctuations up to the point where the mean state is almost fully depleted. Initially the rate of change of fluctuation energy and energy transfer are nearly indistinguishable because of a very weak dissipation rate for total energy. The dissipation rate starts out very small when the fluctuation is dominated by the $k = 2$ baroclinic instability; it is large during the period of forward energy cascade through frontogenesis and small scale instability; and it is weak again during the final stage where the flow is dominated by very large scales.

A primary focus in this paper is on the dynamical differences between QG (balanced) and BOUS solutions, and the implications for the efficiency of energy dissipation by fluctuation currents. The net energy loss in spin-down as a function of $Re$ is shown in Fig. 4. The effective $Re$ for the solutions is a function of resolution; it is diagnosed *a posteriori* through analysis of the combined dissipative effect of the numerical QUICK advection scheme and the explicit Laplacian diffusion. It is clear that for increasing $Re$ the energy dissipation for BOUS approaches a finite asymptotic value. The behavior is markedly different in QG where the net energy loss becomes systematically smaller as $Re$ increases. This indicates that, even though QG dynamics is capable of a certain amount of forward energy cascade for any finite $Re$ value, this route to dissipation has only a limited duration and efficiency when the dissipative scales are moved to higher wavenumbers with increasing $Re$. This is very different for BOUS dynamics, where the forward energy cascade remains efficient enough to reach the dissipative scales even when diffusion moves to smaller scales. This result provides support for the idea that balanced dynamics is limited in its capacity to efficiently dissipate its energy and the idea that unbalanced dynamics is essential for this route to dissipation to be viable at large $Re$. The energy cascades for BOUS and QG will be studied more extensively in Section 4.3.

## 4. Equilibrium

To go beyond the energy loss during a spin-down experiment, we now study equilibrated flows where a sustained energy dissipation balances the energy input. For a given rate of restoring forcing, the solutions are allowed to evolve to a statistically stationary state with an energy input and dissipation balance on average. The mean state is being restored to its basic amplitude with nonzero values for $\alpha_\gamma$ and $\alpha_S$ (Sec. 2). The restoring terms provide a means of sustained energy input into the mean state. The value of $\alpha$ is chosen to equal approximately the growth rate of the most unstable baroclinic-instability mode for the initial mean state. In addition to these mean-state restoring terms, large-scale damping is introduced to remove fluctuation energy at the smallest wavenumbers:

$$partial_t(\hat{u}(k_xk_y), \hat{v}(k_xk_y), \hat{w}(k_xk_y)) = -\alpha_k(\hat{u}(k_xk_y), \hat{v}(k_xk_y), \hat{w}(k_xk_y)) \tag{4.1}$$

when $k_h = \sqrt{(}k_x^2 + k_y^2) < 2$. Here, $(\hat{u}(k_xk_y), \hat{v}(k_xk_y), \hat{w}(k_xk_y))$ are complex amplitudes of $(u, v, w)$ in wavenumber space. This additional damping is introduced to avoid solutions that are dominated by the largest available scales (smallest wavenumbers) due to the ever-present inverse energy cascade in both BOUS and QG. However, the damping coefficient is chosen to be small enough to prevent this form of dissipation to be the primary one. With these considerations, the value is chosen to be $\alpha_k = 0.2$, leading to an almost equal partition between $\mathcal{E}_{kf}$ dissipation at high and low wave numbers for the high-$Re$ BOUS solutions. Since we find that QG has a more efficient inverse energy cascade than BOUS, we choose the larger $\alpha_k = 0.6$ to have the QG equilibrium fluctuation energy generation rate equal to BOUS for high-$Re$ values (Fig. 6). However, independent of the choices for $\alpha_k$, our primary result is robustly true: with high-$Re$ values, the small-scale dissipation efficiency in QG is much less than in BOUS (Fig. 11).

In Fig. 5 time series for total energy are shown for BOUS (left panel) and QG (right panel) during a time period after statistical equilibrium has been established. There is noticeable variability in the mean and fluctuation energy levels, mainly at the timescale of the larger eddies in the solutions. Variations in the total (mean plus fluctuations) energy are much smaller.

Energy diagrams show the very different ways that BOUS and QG manage to equilibrate (Fig. 6). In BOUS the mean state provides a sustained source of energy for the

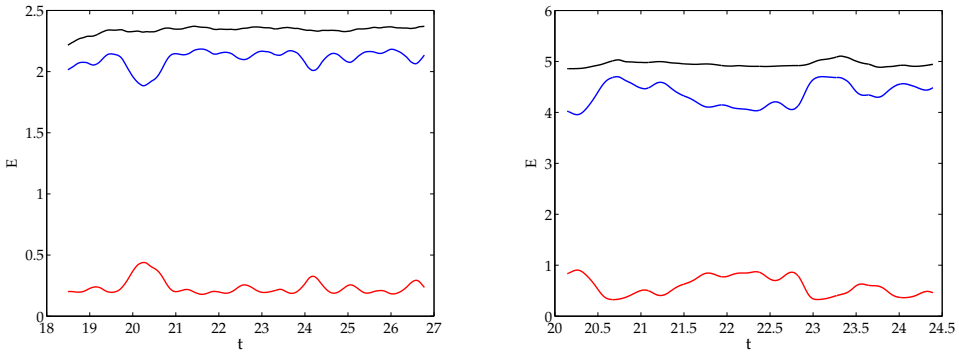


FIGURE 5. Time series of total kinetic plus available potential energy (black) and its mean (red) and fluctuation (blue) components for $Re = 2200$ with restoring forcing during equilibrium: (a) BOUS ($Ro = 0.5$); (b) QG.

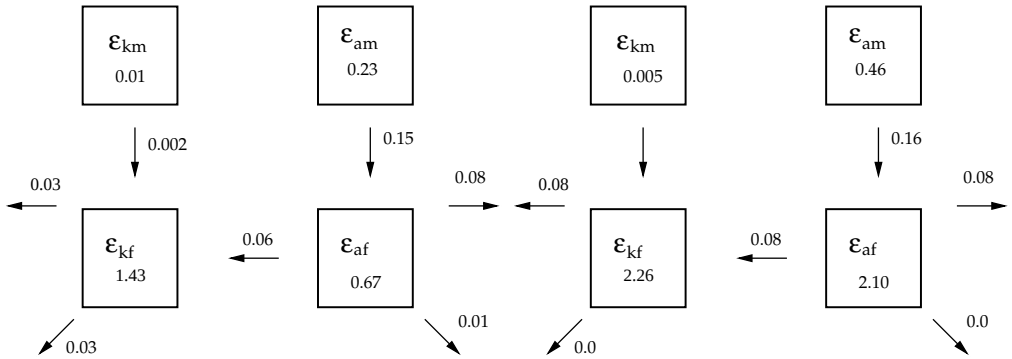


FIGURE 6. Averaged energy balance in equilibrium ($Re = 2200$): (left four boxes) BOUS ($Ro = 0.5$); (right four boxes) QG. All values are scaled with the initial total energy of the basic state $E_0$. The boxes indicate the energy content (*i.e.,* $\mathcal{E}_{km}$ in upper left, $\mathcal{E}_{am}$ in lower left, $\mathcal{E}_{kf}$ in upper right, and $\mathcal{E}_{af}$ in lower right), and the arrows indicate the energy tendencies. Arrows between boxes are conversion terms. Lateral-outward arrows indicate dissipation by the low-wavenumber damping, and diagonal-outward arrows indicate small-scale dissipation. The mean-restoring work arrow is not drawn; its magnitude is equal to the sum of all the energy loss terms.

fluctuations through a horizontal Reynolds stress (0.0002) and through a flux from mean available potential to fluctuation available potential energy (0.15). This is consistent with the interpretation that the main source of energy of the fluctuations is the baroclinic instability of the mean state. About half of the energy that arrives as fluctuation $\mathcal{E}_a$ is removed by restoring sforcing of $\gamma$ and damping of the largest scales of the fluctuations. An additional amount (about 10%) is dissipated as $\mathcal{E}_a$, and the remainder is forcing the fluctuation $\mathcal{E}_k$ through the release of potential energy by the buoyancy flux $\overline{wb}$. From the perspective of $\mathcal{E}_{kf}$, the energy input by Reynolds stress and the release of potential energy is balanced by the damping of low wavenumbers (0.003) and dissipation of $\mathcal{E}_{kf}$ (0.003). For the experiments with high $Re$, the dissipation occurs at increasingly high wavenumber and nonzero dissipation implies a forward cascade of energy (Sec. 4.3). These numbers therefore indicate a sustained forward energy flux that is a significant fraction of the inverse energy cascade. In contrast, the QG solution is characterized by an equilibrium where all the energy put into the fluctuations through the mean state is removed at the smallest wavenumber through the dissipation process. No sustained

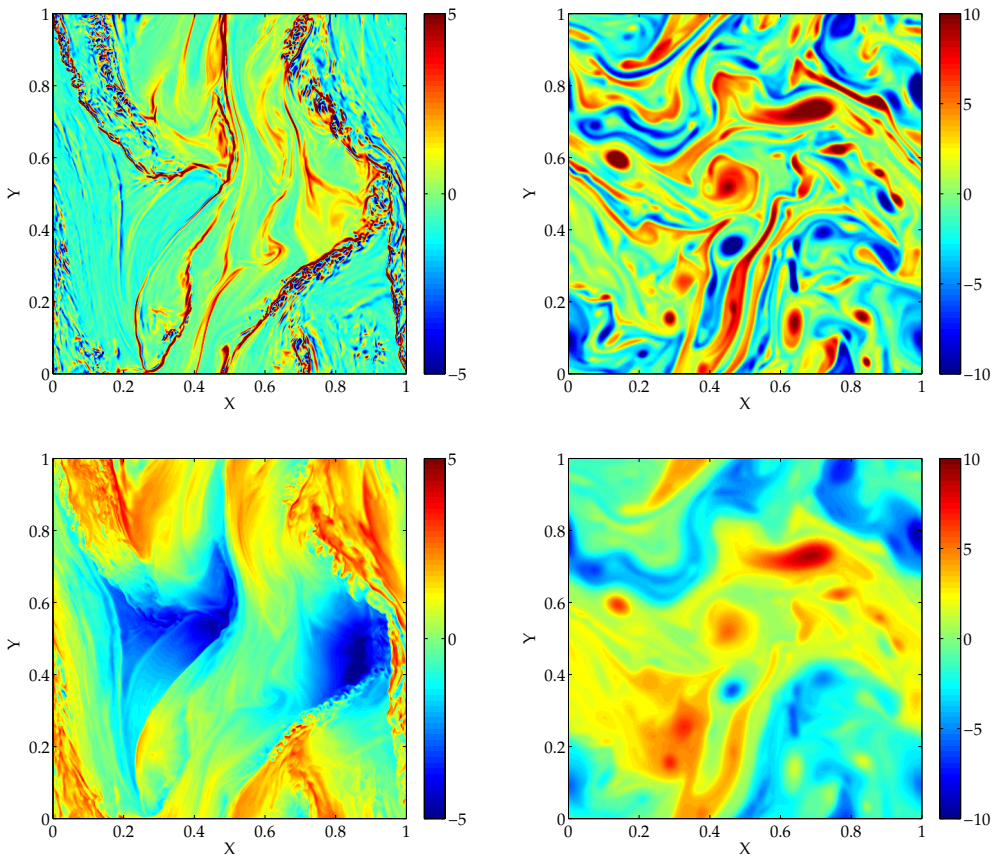


FIGURE 7. Snapshots in equilibrium ($t = 100$) at $z = 0.96$ for $Re = 2200$: BOUS ($Ro = 0.5$) $\zeta^z$ (upper left) and $b$ (lower left); the same for QG in the right panels. Note the fine-structure present in BOUS.

forward energy cascade is established, neither in the kinetic energy, nor in the available potential energy. As a result, no internal dissipation is accomplished in QG, and without the large scale damping, the solution would not be able to equilibrate without having unrealistically large flows. The different types of energy balance and the corresponding fluxes of energy for BOUS and QG implied by Fig. 6 are central to this paper and are further discussed in Secs. 4.2, 4.3, and 5.1.

### 4.1. *Flow Structure: Fronts and Boundary Effects*

Snapshots for $\zeta^z$ and $b$ are shown in Fig. 7 during statistical equilibrium near the upper boundary. For the the vertical component of vorticity, both solutions show filamentation and the occurrence of sharp gradients (*i.e.,* fronts). The difference between BOUS and QG is most evident in the appearance of small-scale fluctuations around frontal regions in BOUS that are absent in QG. The horizontal scale of these BOUS features is very small, about 10% of $L_r$; in Sec. 5.2 we show how they act to limit frontal sharpness.

The horizontally-averaged buoyancy profile during statistical equilibrium for BOUS is plotted in Fig. 8. (The QG solution does not allow for the mean stratification to change from $\gamma = 1$.) Due to the continuing release of potential energy by the fluctuations, the averaged stratification $\gamma$ is larger, by about a factor of 2, than the initial stratification of

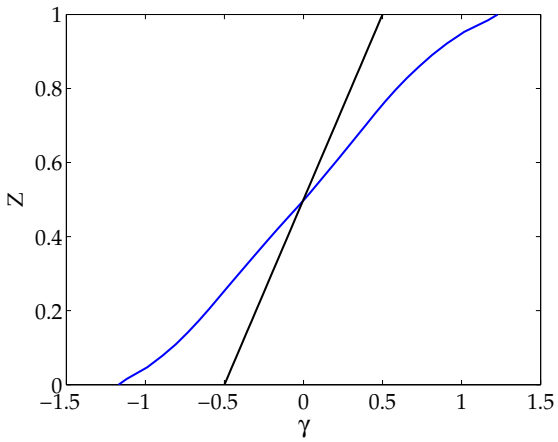


FIGURE 8. Mean buoyancy profile $\int_0^z \gamma\, dz$ in BOUS ($Ro = 0.5$, $Re = 2200$): black is the basic-state stratification (equal to the permanent QG stratification), and blue is the averaged stratification after equilibration.

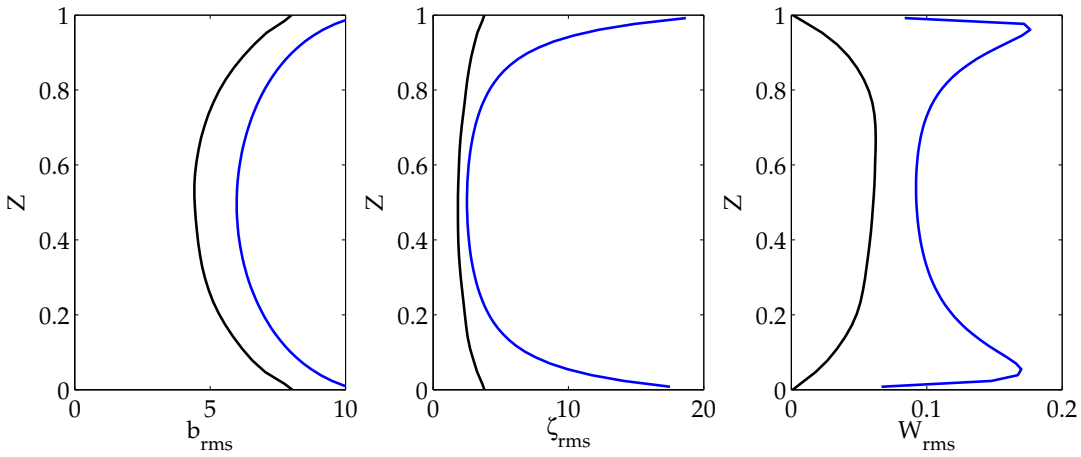


FIGURE 9. Root-mean-square profiles of $b$, $\zeta^z$, and $w$ in equilibrium ($Re = 2200$): BOUS ($Ro = 0.5$, black); QG (blue).

the basic state. Without a restoring term in the $\gamma$ equation (2.5), the average stratification would keep increasing, and this would result in an increasing $L_r$. For large enough $L_r$, the basic state would cease to be unstable to baroclinic instabilities. Evident in the $\gamma$ profile is the moderate increase in stratification near the top and bottom boundary, indicating a modest intensification near the surface. This stratification enhancement accompanies fluctuation intensification near the boundaries in the buoyancy $b$ and vertical vorticity $\zeta^z$ (Fig. 9). On the other hand, even without the stratification enhancement, QG shows a much stronger degree of fluctuation intensification near top and bottom boundaries, especially in $\zeta^z$. This behavior is not uncommon in SQG models where all dynamics arise from the top and bottom surfaces. The profiles of $w_{rms}$ differ even more; QG has a sharp increase of $w_{rms}$ toward the surface, whereas the BOUS $w_{rms}$ smoothly decreases towards zero. Both QG and BOUS show increased frontal activity near the boundary, as indicated by the amplitude for $|\nabla b|$, but for QG the contrast between boundary and interior is much

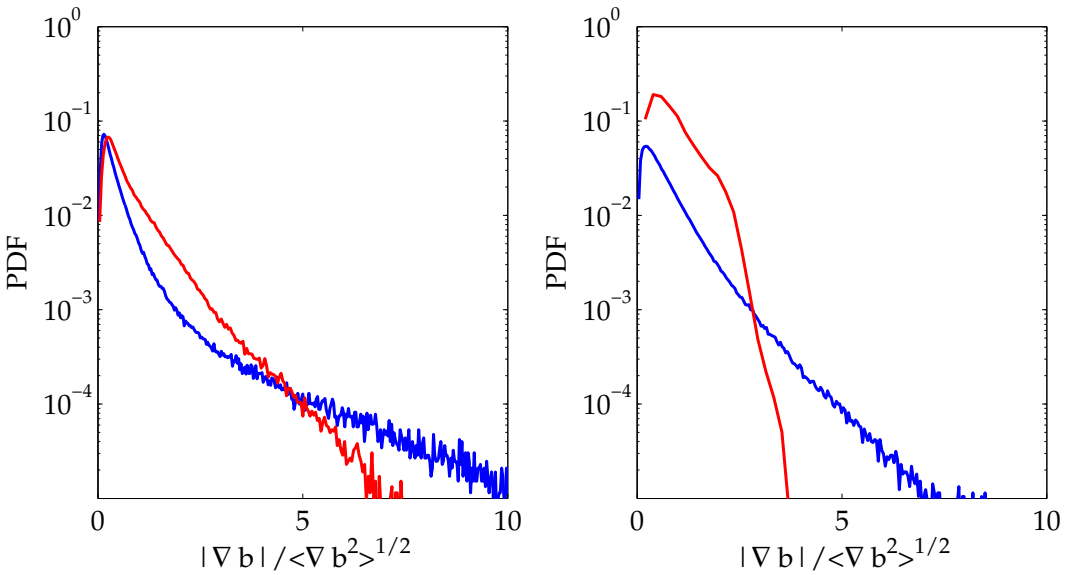


FIGURE 10. PDF of $|\nabla b|$ in the interior (red) and near the boundary (blue) ($Re = 2200$): BOUS ($Ro = 0.5$, left); QG (right). The PDF is normalized to have unit integral and unit variance. The interior is defined as $0.375 < z < 0.625$, and the near-boundary as $z < 0.125$ or $z > 0.875$. Average rms values are $\nabla b_{rms} = 0.51$ (BOUS interior), $\nabla b_{rms} = 1.11$ (BOUS near-boundary), $\nabla b_{rms} = 0.05$ (QG interior), and $\nabla b_{rms} = 1.07$ (QG near-boundary).

more pronounced. Interior $\nabla b_{rms}$ is 50% of its boundary value for BOUS, but it is only 5% of its boundary value for QG. The probability density functions (PDFs) for the strength of buoyancy fronts, as indicated in $|\nabla b|$, are plotted in Fig. 10. The PDFs for BOUS and QG have longer tails near the boundary than in the interior, indicating stronger boundary fronts. For QG there is essentially no interior frontogenesis. Notice that the boundary PDF for BOUS falls off somewhat faster than QG for intermediate frontal amplitudes but extends farther toward extreme amplitudes. This result is consistent with earlier work Held *et al.* (1995) where SQG models do exhibit frontogenetic processes. However, our results demonstrate that the strength of frontogenesis is weaker in QG compared to BOUS.

### 4.2. *Dissipation Efficiency*

An equilibrated flow requires a balance between forcing and dissipation. If the dissipation is to occur at a very small scale, an efficient energy cascade has to be established so that the energy input at large scales can reach the small scales.

We introduce the dissipation efficiency $D_{eff}$ defined by

$$D_{eff} = \frac{\mathcal{D}_f}{\mathcal{E}_{kf}}\,. \tag{4.2}$$

$D_{eff}$ is the volume-integrated, small-scale, fluctuation dissipation rate $\mathcal{D}_f$, due to both viscous and numerical diffusion, divided by the integrated fluctuation kinetic energy $\mathcal{E}_{kf}$. A small value of $D_{eff}$ indicates a solution with a relatively inefficient forward energy cascade and consequently, a poor dissipation efficiency.

Figure 11 plots $D_{eff}$ as a function of $Re$ for BOUS and QG. For small $Re$ values (at courser resolutions), dissipation takes place at scales that are only slightly separated from the forcing on the domain scale and the primary instability near $L_r$. In this regime,

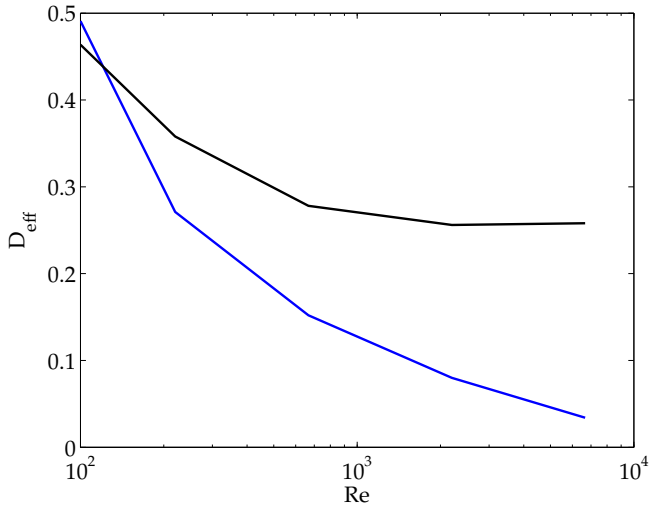


FIGURE 11. Dissipation efficiency as a function of $Re$: BOUS ($Ro = 0.5$; black); QG (blue).

both BOUS and QG show a comparable dissipation efficiency. For increasing $Re$, the dissipation scales are smaller and smaller, and a sustained forward energy cascade needs to be established to reach the dissipation scales. In Fig. 11 we note that QG solutions are increasingly inept at reaching dissipation scales as they move toward smaller and smaller values. In sharp contrast, BOUS is characterized by a forward energy flux that converges toward a constant value for large $Re$ values. This result illustrates several important points. First, in the absence of dissipation near boundaries, BOUS is capable of establishing a direct, sustained route towards dissipation. Second, this direct route is essentially non-balanced (non-QG) in nature. QG, although capable of a certain amount of forward energy cascade, is not able to reach the smallest scales in a sustained way. Therefore, once smaller the submesoscale scales are considered and the dissipation is relegated to smaller and smaller scales, QG dynamics is fundamentally insufficient. The fluctuation available potential energy $\mathcal{E}_{af}$ also has a nonzero energy dissipation in BOUS (Fig. 6). The analogous measure for dissipation efficiency of $\mathcal{E}_{af}$ varies with $Re$ in a similar manner to $D_{eff}$ (Fig. 11).

### 4.3. *Spectral Energy Balance*

To further examine the flow of energy across horizontal scales, we use a spectral representation of the energy balance. This allows for a more quantitative analysis of forward energy flux and dissipation. Equation (2.8) for $\mathcal{E}_{kf}$ is transformed into an equation for $\hat{E}_{kf}(k_x, k_y, z)$, the fluctuation kinetic energy as a function of horizontal wavenumber $(k_x, k_y)$ and $z$ using a 2-dimensional Fourier transform.

$$\frac{1}{2}\frac{\partial \hat{\mathbf{u}} \cdot \hat{\mathbf{u}}^*}{\partial t} = -\hat{\mathbf{u}} \cdot \widehat{(\mathbf{u} \cdot \nabla)\mathbf{u}}^* + \hat{\mathbf{u}} \cdot \widehat{\nabla p}^* + \hat{w} \cdot \hat{b}^* + \hat{\mathbf{u}} \cdot \widehat{\mathbf{D}}^* \,. \tag{4.3}$$

Here $\hat{s}(k_x, k_y, z)$ indicates the complex spectral amplitude. For this analysis the advection term $(\mathbf{u} \cdot \nabla)\mathbf{u}$ is computed using a strictly non-dissipative, centered advection scheme. By recomputing the same advection term using the QUICK advection scheme used in the model and taking the difference, we can compute the numerical dissipation present in the model. This numerical dissipation is added to the explicitly computed dissipation of the form $\mathbf{u} \cdot \nabla^2 \mathbf{u}$, shown in (4.3) as the final term on the right hand side. The second term

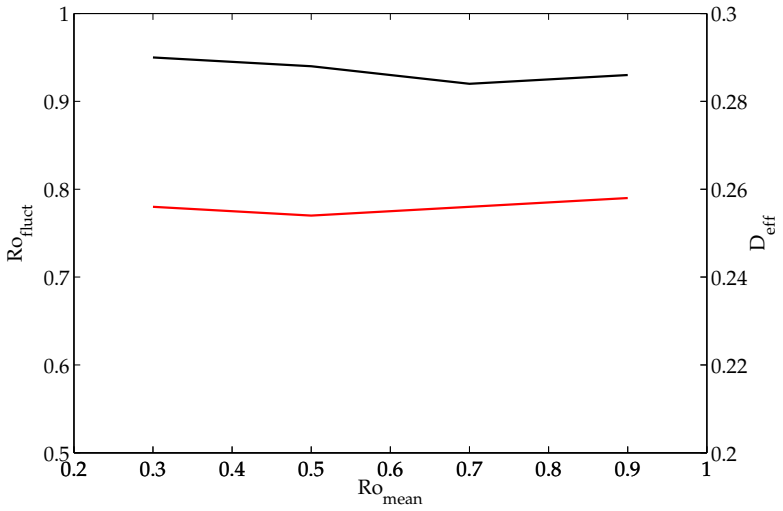


FIGURE 12. Fluctuation Rossby number $Ro_{fluct}$ (measured by the rms value of the non-dimensional fluctuation vertical vorticity multiplied by $Ro$; left ordinate and black curve) and dissipation efficiency (right ordinate and red curve) as functions of mean Rossby number $Ro_{mean} = Ro$. ($Re = 2200$)

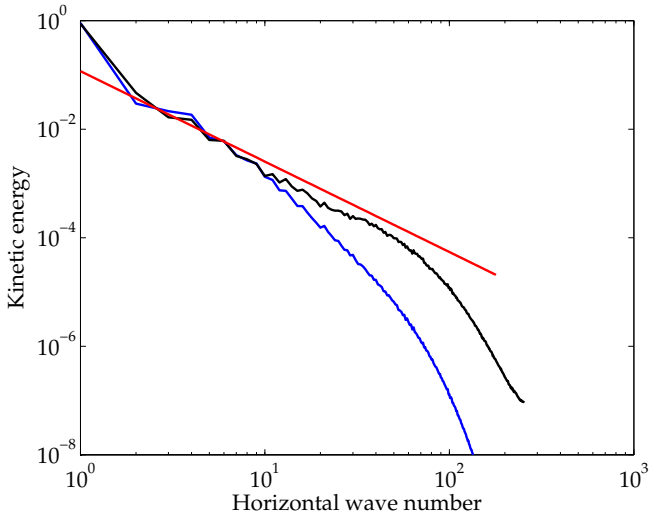


FIGURE 13. Time and depth-averaged horizontal kinetic energy spectrum ($Re = 6600$): BOUS ($Ro = 0.5$, black); QG (blue). A red line $\propto k^{-5/3}$ is plotted for comparison.

on the right-side represents the work done by pressure. For our domain configuration (horizontally periodic with closed top and bottom boundaries), this term is identically zero for every $(k_x, k_y)$ wavenumber when integrated vertically over the full domain. The third right-side term is the release of potential energy by vertical motions. The spectra are vertically domain-integrated and time-averaged and plotted as a function of horizontal wavenumber magnitude, $k_h = \sqrt{(K_x^2 + k_y^2)}$. Both BOUS and QG spectra for $E_{kf}$ have a peak at large scales, where they are quite similar (Fig. 13). The BOUS spectrum decreases more shallowly with $k_h$ than QG, indicating greater submesoscale energy, and

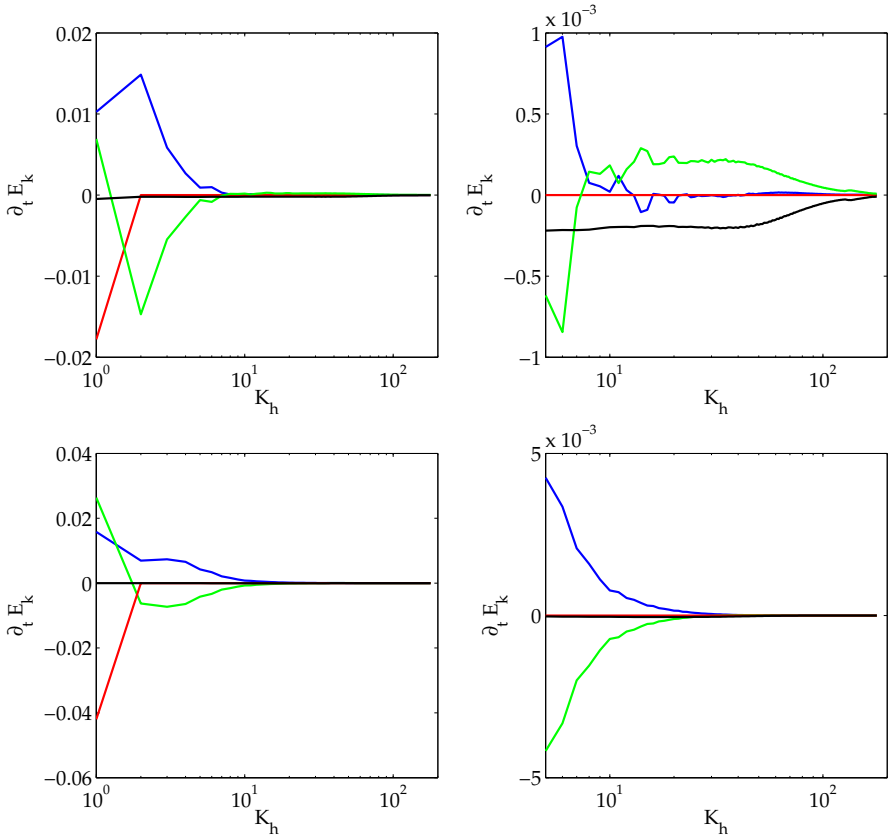


FIGURE 14. Kinetic energy balance in spectral space ($Re = 2200$): BOUS ($Ro = 0.5$, top); QG (bottom). Terms are conversion of potential energy (blue); advective flux divergence (green); restoring damping of wavenumber 1 (red); and dissipation (black). The right panels have an expanded ordinate for the higher wavenumbers.

it approaches the $\sim k_h^{-5/3}$ shape of an anisotropic kinetic-energy inertial range at large $k_h$ (consistent with the forward cascade in Fig. 15).

For smaller wavenumbers the spectral slope of $E_{kf}$ is very similar for both BOUS and QG. For higher wavenumbers the energy spectrum for QG falls off faster than the BOUS spectrum, and at $k_h = 100$ there are two orders of magnitude difference in kinetic energy between the models. These differences in $E_{kf}$ at higher wavenumbers reflect the differences in dissipation efficiency. The individual terms in the spectral energy balance (4.3) are plotted in Fig. 14. The co-spectra are vertically integrated and averaged in time. The sum of these terms was compared to the accumulated change of kinetic energy $\hat{E}_{kf} = 1/2\hat{\mathbf{u}} \cdot \hat{\mathbf{u}}$ during the averaging period to verify correctness of the balance and to verify that the time-averaged trend in $\hat{E}_{kf}(k_h)$ is small compared to individual terms in the balance. The top panels are the BOUS results, and the lower panels are QG. In red, the effect of the damping at $k_h = 1$ is shown. As expected, the damping provides a sink for $E_{kf}$, acting exclusively at $k_h = 1$. The blue line is the release of potential energy, and it has a peak at $k_h = 2$ for BOUS, and $k_h = 3$ for QG, corresponding to the most unstable baroclinically unstable mode of the basic states. QG has an even stronger peak at $k_h = 1$. This results from the fact that there is a very large amount of energy in the $k_h = 1$ spectral component. Even though that mode is less effective in releasing potential energy than

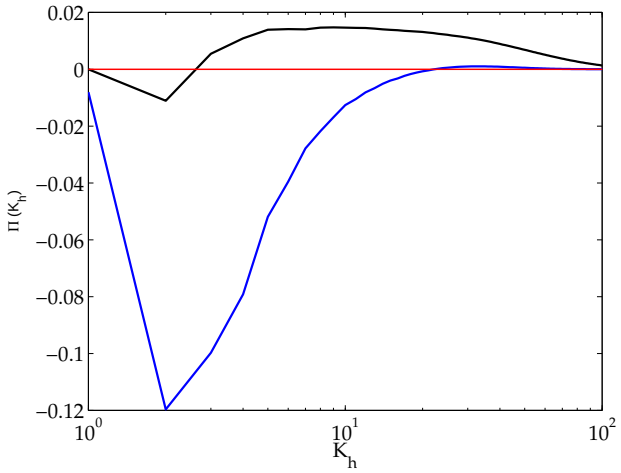


FIGURE 15. Spectral flux of kinetic energy ($Re = 6600$): BOUS ($Ro = 0.5$, black); QG (blue). Note the forward cascade for BOUS and inverse cascade for QG.

the most unstable mode at slightly higher wavenumbers, it still releases more potential energy in an absolute sense. The green line is the the effect of the momentum-advection term. When integrated over the wavenumber range, this term is identically zero, so it provides only a redistribution of energy across wavenumbers. With this information we can interpret the balance of $E_{kf}$ at $k_h = 1$. Both BOUS and QG release potential energy at that wavenumber, and in addition both solutions show an inverse energy cascade: energy is transferred from higher wavenumbers by means of the advective term. These two sources of energy are balanced by the large-scale damping. The right panels in Fig. 14 display the spectral energy balance for an expanded wavenumber ordinate at large $k_h$. There the diffusive term is visibly nonzero for BOUS. BOUS shows that release of potential energy becomes negligible for $K_h > 20$, where dissipation balances the energy that is forward-transferred by the advective terms. QG provides a very different picture for energy equilibration: the release of potential energy at relatively small wavenumbers is balanced by an inverse energy cascade, and the small-scale dissipation remains very small.

The energy cascade can be expressed explicitly in terms of a spectral kinetic-energy flux $\Pi$ defined by

$$\Pi(k_h) = -\int_{k=0}^{k=k_h} \hat{\mathbf{u}} \cdot (\widehat{\mathbf{u} \cdot \nabla})\mathbf{u}^* \, dk \,. \tag{4.4}$$

Since advection is purely a redistribution term over wavenumbers, its wavenumber-integrated effect must be zero when computed correctly; hence $\Pi(0) = \Pi(k_{max}) = 0$. Both BOUS and QG $\Pi(k_h)$ curves show a negative (inverse) energy flux for small wavenumbers (Fig. 15). For higher wavenumbers ($k_h > 3$) the results significantly differ: BOUS has a consistent forward energy flux, nearly constant for a range up to $k_h = 20$ (as in a kinetic-energy inertial range), while QG has a negative energy flux (inverse cascade) for all wavenumbers. These curves are consistent with earlier remarks that QG is incapable of reaching dissipation scales at large $Re$. In contrast, BOUS is characterized by a sustained forward energy cascade, allowing for a dissipation efficiency that becomes independent of the Reynolds number $Re$ for large $Re$.

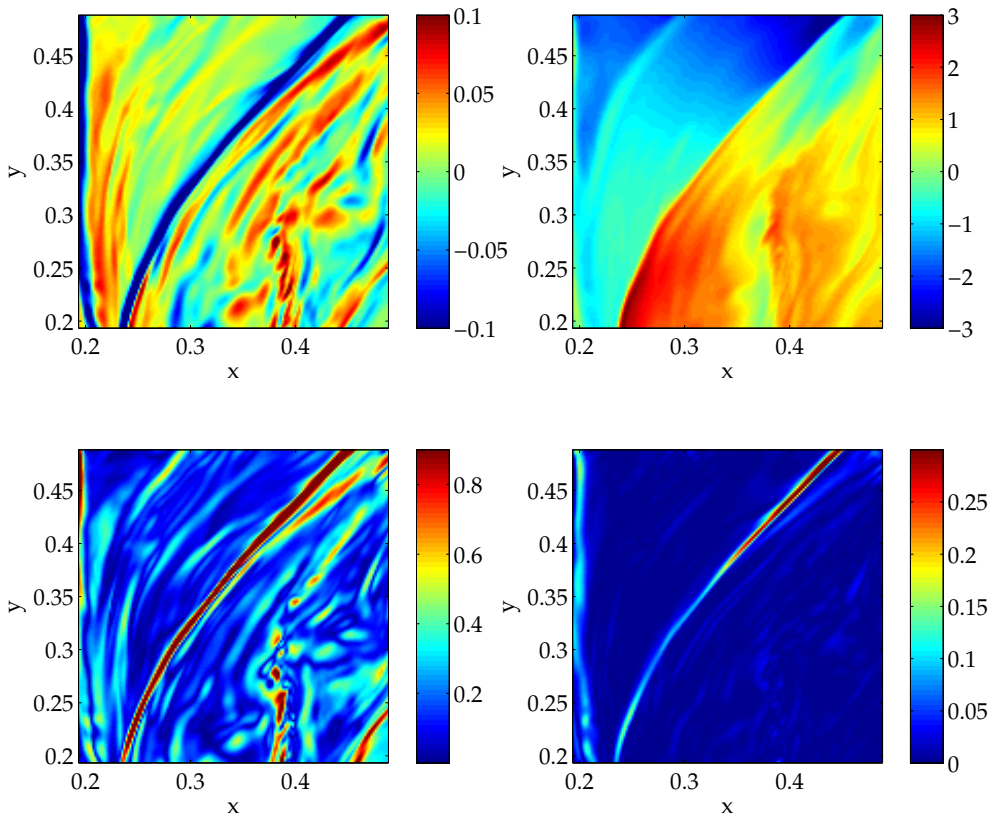


FIGURE 16. A local region with $\sim$ stable submesoscale frontogenesis in BOUS ($z = 0.96$, $Ro = 0.5$, $Re = 6600$): (upper left) vertical velocity; (upper right) buoyancy; (lower left) error in gradient wind balance $\epsilon_{gw}$; (lower right) error in hydrostatic balance $\epsilon_{hydro}$.

## 5. Unbalanced Flow

A central issue is the degree to which the BOUS flow satisfies a diagnostic force balance. The more general horizontal force balance is gradient-wind balance, where Coriolis force, pressure-gradient force, and the advective centrifugal force in curved flows provide the dominant terms in the divergence of the horizontal momentum equation (McWilliams 1985):

$$-\nabla\cdot(\mathbf{u}_h\cdot\nabla_h\mathbf{u}_h)+f\zeta^z=\frac{1}{\rho}\nabla_h^2 p\,. \tag{5.1}$$

We assess the degree of balance in our solutions as the departure from (5.1) suitably normalized to provide a relative measure:

$$\epsilon_{gw}(\mathbf{x},t)=\frac{\left|\nabla\cdot(\mathbf{u}_h\cdot\nabla_h\mathbf{u}_h)-f\zeta^z+\frac{1}{\rho}\nabla_h^2 p\right|}{|\nabla\cdot(\mathbf{u}_h\cdot\nabla_h\mathbf{u}_h)|+f|\zeta^z|+|\frac{1}{\rho}\nabla_h^2 p|+\mu}\,. \tag{5.2}$$

$\mu = f\zeta^z_{rms} + |\frac{1}{\rho}(\nabla_h^2 p)_{rms}$ is added to the denominator to exclude situations with locally weak force divergences from being identified as significantly unbalanced. The degree of

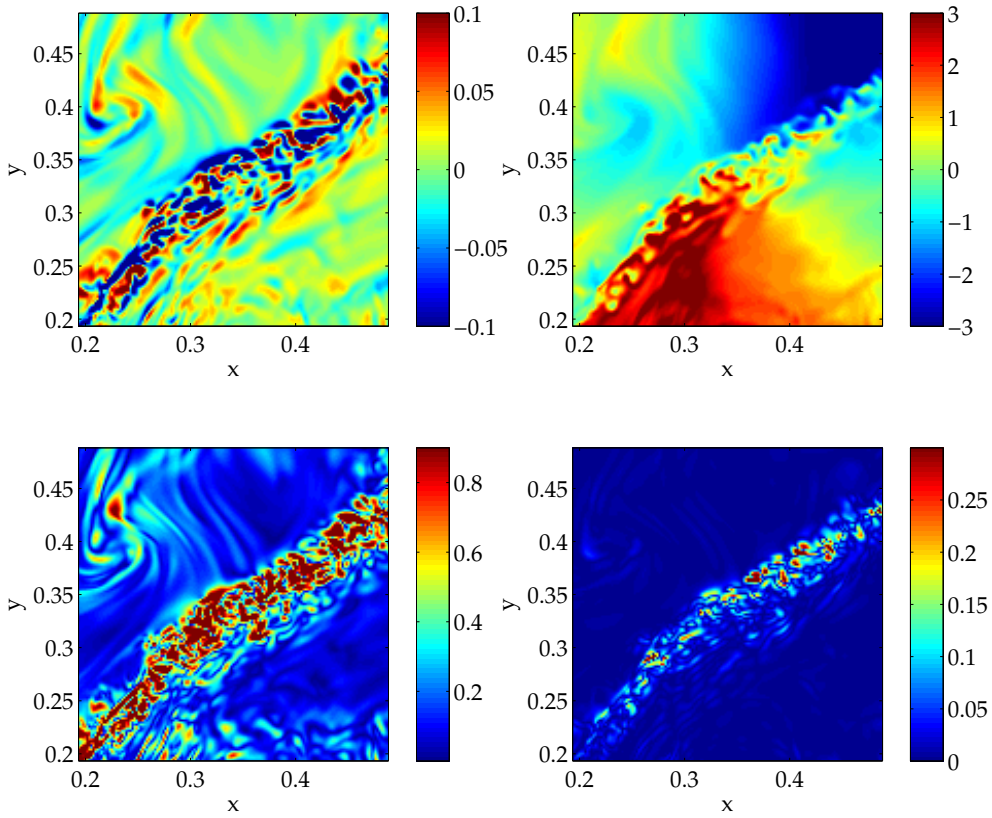


FIGURE 17. A local region with submesoscale frontal instability in BOUS ($z = 0.96$, $Ro = 0.5$, $Re = 6600$). The format is the same as in Fig. 16.

unbalance thus lies between $\epsilon \approx 0$ (highly balanced or weak) and $\epsilon \approx 1$ (fully unbalanced). An alternative, less restrictive, measure of unbalance based on geostrophic balance is

$$\epsilon_{geo}(\mathbf{x}, t) = \frac{\left| f\zeta^z - \frac{1}{\rho}\nabla_h^2 p \right|}{f|\zeta^z| + |\frac{1}{\rho}\nabla_h^2 p| + \mu}\,, \tag{5.3}$$

but this fails to recognize strong vortices as balanced by excluding the centrifugal force divergence included in (5.2). An analogous measure to assess the degree to which the solutions are in hydrostatic balance is

$$\epsilon_{hydro}(\mathbf{x}, t) = \frac{|-\partial_z p + b|}{|\partial^z p| + |b| + \mu}\,. \tag{5.4}$$

For (5.4), $\mu = (\partial^z p)_{rms} + b_{rms}$ is added to the denominator.

$\epsilon_{gw}$ and $\epsilon_{hydro}$ for the BOUS solutions indicate that the flow, in most places, is highly balanced. This is seen in Fig. 16, a snapshot of a local region around a stable front. Outside the frontal region the solution is to a high degree in both gradient-wind balance and hydrostatic balance. However, at the front, large unbalance is evident. This unbalance is consistent with an inherently unbalanced secondary circulation around a front that

is undergoing active frontogenesis (Hoskins and Bretherton 1972). A buoyancy gradient that is being strengthened through the influence of a larger scale straining field undergoes geostrophic adjustment by means of a restratifying secondary flow, comprised of upwelling (downwelling) on the more (less) buoyant side of the front. This circulation is clearly evident in Fig. 16 in vertical velocity $w$ with significant unbalance in $\epsilon_{gw}$. In general the flow is almost perfectly in hydrostatic balance except for a small part of the front.

Figure 17 is an analogous depiction for another frontal region that is actively unstable as evidenced by the abundance of small-scale features. This instability limits the degree to which the front may be further sharpened by a larger-scale straining field. This small scale frontal instability enhances both vertical and horizontal mixing (Sec. 5.2). The small-scale motions exhibit significant gradient-wind and hydrostatic unbalance.

During spin-down (Sec. 3), the solutions have similar spatial patterns and degrees of unbalance. In the late stages of spin-down (*e.g.,* Fig. 2), the solutions are in nearly perfect gradient-wind and hydrostatic balance. This is a result of a cessation of active generation of new fluctuations and the completed dissipation of all unbalanced motions.

### 5.1. *Energy Cascade*

The comparison between QG and BOUS solutions demonstrates a dramatic difference in the ability to establish a forward cascade route towards dissipation. While QG turbulence is characterized by an inverse energy cascade Charney (1971), the BOUS equations evidently provide for the possibility of a forward cascade. Our experiments show that, even when most of the BOUS solutions is in balance — even the simpler geostrophic balance — the flow generates sufficient unbalanced motions to initiate a forward energy cascade.

A formal decomposition of a solution into balanced and unbalanced components is a topic of continuing debate. It is not yet clear that such a split will have a meaningfully unique answer. However, a simplest approximation for such a split is to orthogonally project the full velocity field of the BOUS solutions $\mathbf{u}$ onto a velocity field $\mathbf{u}_{nd}$ that is horizontally non-divergent, $\nabla_h \cdot \mathbf{u}_{nd} = 0$. This projection matches the property that geostrophic velocity is non-divergent. The left panel of Fig. 18 is the kinetic energy spectra for $\mathbf{u}$ and $\mathbf{u}_{nd}$. As expected, for smaller wavenumbers the energies in $\mathbf{u}$ and $\mathbf{u}_{nd}$ are indistinguishable, while for larger wavenumbers the energy in the unbalanced field may be as much as 50 % of the total energy spectrum, *i.e.,* an approximate equipartition between balanced and unbalanced parts of the flow. The wavenumber-integrated energy contained in the unbalanced flow is only about 2 % of the total.

The energy flux across wave numbers $\Pi$ (Sec. 4.3) is shown in the right panel of Fig. 18, both for the full BOUS solution (as in Fig. 14) and for the momentum advection associated only with $\mathbf{u}_{nd}$ (approximating the flux associated with the balanced part of the flow). It is clear that the forward energy cascade depends on the unbalanced flow in an essential way. The balanced flow leads to a flux $\Pi$ that is almost completely inverted, sending energy towards larger scales, identical to the QG solutions. This demonstrates that even when a flow is mostly balanced, as here and in oceanic mesoscale flows, the unbalanced motions may only represent a small fraction of the flows energy, but the motions still have a crucial role in establishing a forward kinetic energy cascade to reach smaller scales where dissipation occurs.

A recent study of subtropical eastern boundary currents also finds a forward kinetic energy cascade in the submesoscale wavenumber range (Capet *et al.* 2007a). However, in that study the size of the advection term relative to the energy released by potential energy at high wavenumbers is relatively small, whereas the Eady flow has a much more developed forward cascade extending beyond the wavenumbers of significant potential

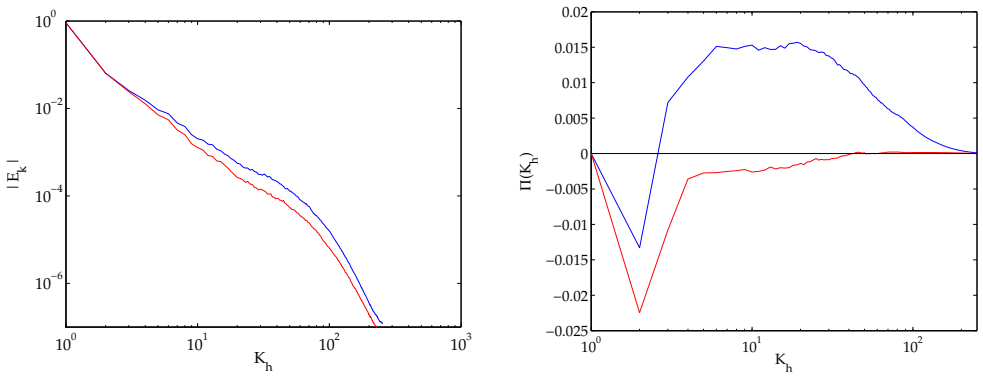


FIGURE 18. Left panel: 3D kinetic energy spectrum of $\mathbf{u}$ for the BOUS solution (blue) and its horizontally non-divergent counterpart $\mathbf{u}_{nd}$ (red). Right panel: spectral flux of kinetic energy for BOUS velocity (black) and for a projected horizontal velocity with $\nabla_h \cdot \mathbf{u}_h = 0$ (red). ($Ro = 0.5$; $Re = 6600$.)

energy conversion. We would expect that the flow regime in Capet *et al.* (2007a) would develop a dominant forward cascade for sufficiently high grid resolution.

### 5.2. *Fine-Scale Instability*

For the fluctuations in the BOUS solutions, we can clearly identify two distinct types of instability. At the largest scales fluctuations arise through baroclinic instability of the mean vertical-shear flow, and as they grow they act to limit its strength. Additionally, a small-scale frontal instability arises and limits the ability of the mesoscale strain field to continue to sharpen the front (*cf.,* Figs. 5 and 17). The latter is likely to play an important role in the forward kinetic energy cascade.

We focus on a quasi-rectilinear, unstable front to investigate the energy balance for the frontal instabilities by computing energy conversion terms for the local fluctuations relative to the parallel frontal flow. For this purpose we define a locally rotated reference frame with its $y_*$ axis aligned with the front. The local coordinates are $x_*$ and $y_*$ in the cross- and along-front directions with horizontal velocities $u_*$ and $v_*$. The front is located at $x_* = 0$. Figure 19 depicts an unstable front in these local coordinates. The vertical velocity is generally downward on the less buoyant side of the front, consistent with a secondary frontogenetic circulation. The secondary circulation pattern is also evident in the lower-right panel where along-front averaged velocity vectors are overlaid on the averaged buoyancy field. In addition, a pattern of up- and downward velocity is seen in the fluctuations, indicating an unstable frontal mode. The horizontal slice of buoyancy overlaid with horizontal velocity vectors (upper-right panel) indicates that the strong frontal buoyancy gradient coincides with an accompanying horizontal divergence.

The local mean $\overline{\cdot}$ is defined as the along-front average, and perturbations to the local mean are denoted with $\cdot'$. Figure 20 plots the energy conversion terms for the fluctuation kinetic energy balance: the horizontal Reynolds stress $\overline{(u'_* v'_*)\overline{v_*}_x}$; the vertical Reynolds stress $\overline{(WV'_*)\overline{v_*}_z}$; and the conversion of potential energy $\overline{(Wb')}$. In addition, the figure plots the conversion of potential energy by the along-front averaged flow $\overline{w}\overline{b}$. From these $x_*$ and $z_*$ profiles, it is clear that the instability arises mostly from the horizontal shear of the frontal flow and to a lesser extent its vertical shear. Most of the energy conversion is near the surface where the velocity shear is largest. Conversion of potential energy is

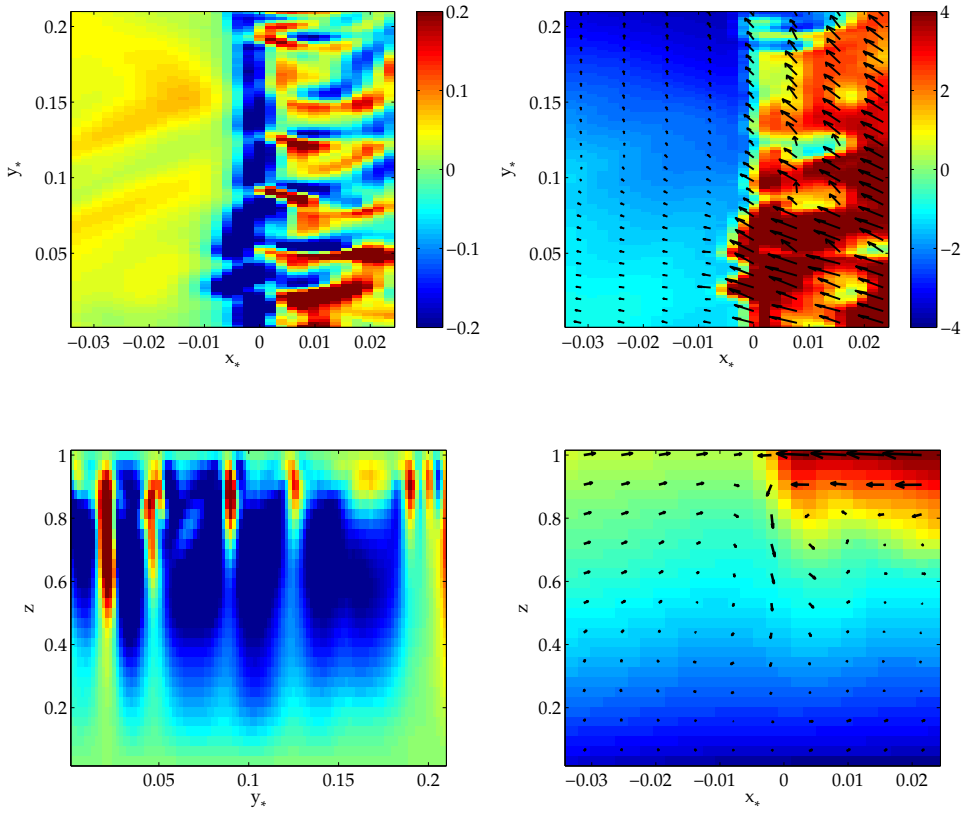


FIGURE 19. A local view of an unstable frontal region. Upper-left: near-surface, horizontal slice for vertical velocity. Upper-right: the same for buoyancy with overlaid horizontal velocity vectors. Lower-left: vertical, along-frontal section for vertical velocity at $x_* = 0$. Lower-right: vertical, cross-frontal section of along-front averaged buoyancy and velocity vectors. The local volume-averaged velocity has been subtracted from $\mathbf{v}$ to expose the frontal circulation.

unimportant for the local energy balance, consistent with its disappearance of $\hat{w}\hat{b}*$ at high wavenumbers in Fig. 14.

Recently, other studies on submesoscale instabilities find that they arise by the release of potential energy rather than horizontal Reynolds stress (*i.e.,* a baroclinic instability; Capet *et al.* (2007b); Boccaletti *et al.* (2007)). One difference between those studies and the current one is the absence here of a surface mixed-layer with its reduced vertical gradients. Such an layer introduces a separate, much smaller, mixed-layer deformation radius, implying possible baroclinic instability on a smaller horizontal scale (Capet *et al.* 2007b). Furthermore, the enhanced vertical mixing in such a surface mixed-layer may alter the potential for different types of instabilities. These various influences on submesoscale and frontal instabilities are not yet fully understood. Another relevant study without a surface mixed-layer (Klein *et al.* 2007) finds no evidence of a shear-driven frontal instability. A plausible explanation is that, relative to the first-baroclinic deformation radius, our simulations have finer resolution, allowing the fronts to sharpen further until a horizontal shear instability arises.

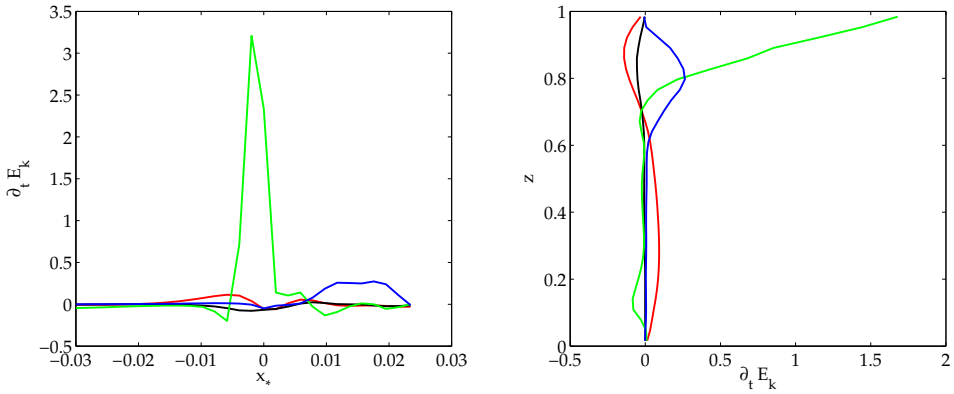


FIGURE 20. Energetics of the frontal instability in Fig. 19. (Left) cross-frontal profiles for depth-averaged kinetic-energy production terms, and (Right) vertical profiles averaged over the cross-frontal direction. The production terms are $\overline{(u'_* v'_*)\overline{v_*}_x}$ (green), $\overline{(WV'_*)\overline{v_*}_z}$ (blue), $\overline{(Wb')}$ (black), and $\overline{w}\overline{b}$ (red).

## 6. Summary

We have demonstrated that, in absence of other means of dissipation such as in turbulent boundary layers, a Boussinesq flow is capable of establishing a direct route towards dissipation by means of unbalanced motions and a forward energy cascade. In contrast, a Quasigeostrophic flow that by its very nature cannot represent unbalanced motions is markedly incapable of establishing such a direct route and is increasingly non-dissipative for increasing Reynolds number. The Boussinesq flow is energetically dominated by balanced flow, both with regard to gradient-wind balance and even more so to hydrostatic balance. However, the flow develops sharp frontal regions on small scales where locally the fluctuation Rossby number is not small and unbalanced motions emerge. The unbalance in the frontal regions is due to both secondary circulation associated with frontogenesis and to frontal instabilities. The frontal instabilities arise primarily from the horizontal shear of the along-front velocity profiles. This means that these unstable modes are neither baroclinic nor convective in their dynamical generation. Unbalanced motions are essential in establishing dissipation by means of a forward energy cascade, as demonstrated by a decomposition of the flow into horizontally non-divergent ($\sim$ balanced) and divergent ($\sim$ unbalanced) components. The unbalanced motions represent only a small fraction of the total kinetic energy of the flow, yet they are essential to the forward energy cascade *en route* to dissipation. As expected from geostrophic turbulence theory, the balanced motions provide an inverse energy cascade toward larger scales and contribute little energy dissipation in the interior region of the flow.

Acknowledgments We appreciate the support of the National Science Foundation through grants OCE 02-21177 and OCE 05-50227.

## REFERENCES

Boccaletti, G., Ferrari, R., and Fox-Kemper, B. (2007). Mixed layer instabilities and restratification. Submitted to *J. Phys. Ocean.*

Capet, X., McWilliams, M., Molemaker, M., and Shepetkin, A. (2007a). Mesoscale to submesoscale transition in the California Current System: Energy balance and flux. Submitted to *J. Phys. Ocean.*

Capet, X., McWilliams, M., Molemaker, M., and Shepetkin, A. (2007b). Mesoscale to subme-

soscale transition in the California Current System: Frontal processes. Accepted by *J. Phys. Ocean.*

Charney, J. (1971). Geostrophic turbulence. *J. Atmos. Sci.*, **28**, 1087–1095.

Eady, E. (1949). Long waves and cyclone waves. *Tellus*, **1**, 33–52.

Held, I., Pierrehumbert, R., Garner, S., and Swanson, K. (1995). Surface quasi-geostrophic dynamics. *J. Fluid Mech.*, **282**, 1–20.

Hoskins, B. and Bretherton, F. (1972). Atmospheric frontogenesis models: Mathematical formulation and solution. *J. Atmos. Sci.*, **29**, 11–37.

Klein, P., Bach, L., Lapeyre, G., Capet, X., and LE Gentil, S. (2007). Upper ocean turbulence from high resolution 3-D simulation. Submitted to *J. Phys. Ocean.*

Leonard, B. P. (1979). A stable and accurate convective modelling procedure based on quadratic upstream interpolation. *Comput. Meth. Appl. Mech. Eng.*, **19**, 59–98.

Lindborg, E. (2005). The effect of rotation on the mesoscale energy cascade in the free atmosphere. *grl*, **19**, 59–98.

Lorenz, E. (1955). Available energy and the maintenance of the general circulation. *Tellus*, **7**, 157–167.

McWilliams, J. (1985). A note on a uniformly valid model spanning the regimes of geostrophic and isotropic, stratified turbulence: balanced turbulence. *J. Atmos. Sci.*, **42**, 1773–1774.

McWilliams, J. (2003). Diagnostic force balance and its limits. In O. Velasco Fuentes, J. Sheinbaum, and J. Ochoa, editors, *Nonlinear Processes in Geophysical Fluid Dynamics*, pages 287–304. Kluwer Academic Publishers.

Molemaker, M. and Dijkstra, H. (2000). Stability of a cold-core eddy in the presence of convection: Hydrostatic versus non-hydrostatic modeling. *J. Phys. Ocean.*, **30**, 475–494.

Molemaker, M. and McWilliams (2008). Accurate calculation of available potential energy budgets in finite-difference models. Submitted to *J. Fluid Mechanics*.

Molemaker, M. and Vilá-Guerau de Arellano, J. (1998). Control of chemical reactions by convective turbulence in the boundary layer. *J. Atmos. Sci.*, **55**, 568–579.

Molemaker, M., J.C. McWilliams, J., and Yavneh, I. (2000). Instability and equilibration of centrifugally-stable stratified Taylor-Couette flow. *Phys. Rev. Lett.*, **86**, 5270–5273.

Molemaker, M., McWilliams, J., and Yavneh, I. (2005). Baroclinic instability and loss of balance. *J. Phys. Ocean.*, **35**, 1505–1517.

Muller, P., McWilliams, J., and Molemaker, M. (2005). Routes to dissipation in the ocean: the 2d/3d turbulence conundrum. In H. Baumert, J. Simpson, and J. Sundermann, editors, *Marine Turbulence: Theories, Observations and Models*, pages 397–405. Cambridge Press.

Pedlosky, J. (1987). *Geophysical Fluid Dynamics*. Springer-Verlag.

Press, W., Flannery, B., Teukolsky, S., and Vetterling, W. (1986). *Numerical Recipes*. Cambridge University Press.

Rhines, P. and Young, W. (1982). Homogenization of potential vorticity in planetary gyres. *jfm*, **122**, 347–367.

Shchepetkin, A. and McWilliams, J. (1998). Quasi-monotone advection schemes based on explicit locally adaptive dissipation. *Monthly Weather Review*, **126**, 1541–1580.

Stone, P. (1966). On non-geostrophic baroclinic instability. *J. Atmos. Sci.*, **23**, 390–400.

Stone, P. (1970). On non-geostrophic baroclinic instability: Part II. *J. Atmos. Sci.*, **27**, 721–726.

Waite, M. and Bartello, P. (2006). The transition from geostrophic to stratified turbulence. *J. Fluid Mech.*, **568**, 89–108.

Winters, K., Lombard, P., Riley, J., and D'Asaro, E. (1995). Available potential energy and mixing in density-stratified fluids. *J. Fluid Mech.*, **289**, 115–128.